A Systematic Method for Efficient Wireless Powering to Implantable Biomedical Devices

Xianbo Cao, *Graduate Student Member, IEEE*, Hiroyasu Sato, *Member, IEEE*,
Kai-Da Xu, *Senior Member, IEEE*, Wen Jiang, *Member, IEEE*, Shuxi Gong, *Member, IEEE*,
and Qiang Chen, *Senior Member, IEEE*

Abstract— Wireless power transfer (WPT) technology has played a vital role in the rapid development of biomedical devices. While several single methods to improve WPT efficiency have been reported, the lack of integrality in these single methods limits the effect of the improvements. In this investigation, we analyze the physical process of a typical WPT scenario and find that the high propagation loss consisting of in-tissue attenuation and interface reflection degrades the WPT performance. A systematic method to comprehensively improve WPT efficiency is then proposed. Specifically, a Fresnel zone plate (FZP) is applied against the attenuation of inner biological tissue, and a practical air layer-artificial matching layer (AL-AML) is applied to decrease the reflection on the surface of biological tissue. According to a simulation of possible analytical models, the efficiency is significantly improved when using the proposed method. In an experiment with an implant depth of 20 mm, the proposed systematic method is found to enhance maximum relative received power by 12 dB, with an almost 15-fold increase in efficiency over the conventional system with just a transmitter (Tx) and a receiver (Rx). It is also verified that the improvement in efficiency is greater in the systematic method than in single methods. Also, various misalignment tolerances between the proposed structures and the Rx are determined from the coupling strength of the proposed WPT system. The results of this investigation show the potential of the proposed systematic method for further improvements in WPT efficiency.

Index Terms— Implantable, propagation loss, systematic method, wireless power transfer (WPT).

I. INTRODUCTION

IN RECENT years, implantable medical devices for sensing, drug delivery, and local stimulation have played an increasingly important role in modern medical treatments.
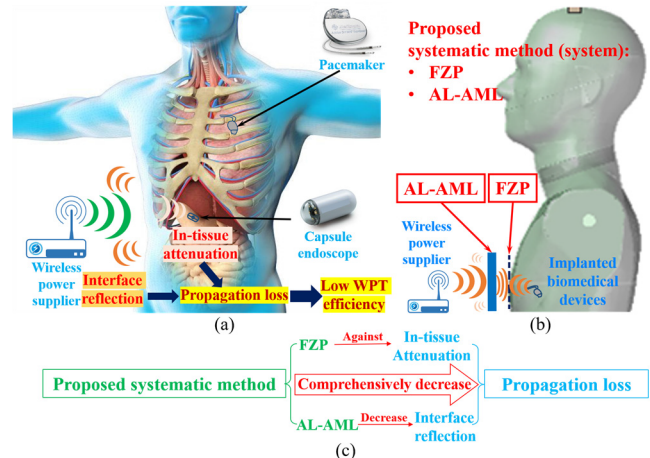

Fig. 1. Typical scenarios of WPT technology applied to implantable biomedical devices. (a) High propagation loss occurs in the WPT process. (b) Proposed systematic method for improving WPT efficiency. (c) Design principle of the proposed systematic method.

These devices help to facilitate the management of medical disorders over a broad range of applications through preventive and postsurgery monitoring [1]. However, there are problems and risks, which have yet to be successfully addressed, including battery leakage, battery exhaustion, and replacement challenges. Wireless power transfer (WPT) as an implantable power supply has been given considerable research attention in recent years as means of enabling the miniaturization of implantable devices [2]. Fig. 1(a) shows typical scenarios of wireless powering into biomedical devices: the wireless powering of a pacemaker and a capsule endoscope.

Most of the investigations on the wireless delivery of energy to implantable devices have been operated in the low-frequency range (kHz–MHz). In low-frequency environments, most transmitted energy is stored in fields rather than by radiation. The wireless link between transmitter (Tx) and receiver (Rx) can be classified as electromagnetic (EM) coupling [3], [4], [5], [6] and magnetic resonance coupling [7], [8], [9], [10], [11], [12], [13] based on EM near-field coupling and the share of magnetic flux, respectively. In these studies, the Tx and Rx usually adopt coils and printed spiral antennas. The main attempt is to design the configuration of coils to improve transfer efficiency. In a recently reported new method for charging an implantable

Xianbo Cao, Hiroyasu Sato, and Qiang Chen are with the Department of Communications Engineering, Tohoku University, Sendai 980-8579, Japan (e-mail: cao.xianbo.s7@dc.tohoku.ac.jp).

Kai-Da Xu was with the Department of Communications Engineering, Tohoku University, Sendai 980-8579, Japan. He is now with the School of Information and Communications Engineering, Xi'an Jiaotong University, Xi'an 710049, China (e-mail: kaidaxu@ieee.org).

Wen Jiang and Shuxi Gong are with the National Key Laboratory of Antennas and Microwave Technology, Xidian University, Xi'an 710071, China.

cardiac pacemaker [13], a well-designed double sandwiched structure for both Tx and Rx is proposed to improve the efficiency of the WPT system. However, because the system is operated at 160 kHz, the Rx coil is as large as the pacemaker. Recently, metasurfaces have been employed to improve the performance of the wireless power link [14], [15], [16]. For instance, the negative-permeability metasurface integrated into the WPT system in a recent study by Li et al. [16] consists of a conformal magnetic resonator Tx coil and a dual-band Rx coil. By utilizing a negative-permeability metasurface, the WPT system working at 430 MHz in their study was reported to achieve a further operation distance and a coupling enhancement of up to 15.7 dB. However, the large size of the coils limits their application in implantable devices and presents a severe challenge to near-field coupling technology at the low-frequency range [2].

Recently, WPT systems with operation frequencies from the sub-GHz to the low GHz range have been attracting more attention due to their higher transfer efficiency and potential for dramatic miniaturization [17], [18], [19], [20], [21], [22], [23], [24], [25], [26]. In a study on the optimal frequencies of different types of biological tissue by Poon et al. [17], when the dimension of the transmit antenna is much smaller than the wavelength in the GHz range, the optimal frequency was found to be in the GHz range, and when the dimension is similar to the wavelength in the sub-GHz range, the optimal frequency was found to be in the sub-GHz range. In an experiment performed on a live pig to analyze the propagation loss of RF signal for in-body to in-body implants [20], an ISM radio band frequency range between 2.4 and 2.5 GHz was found to be optimal for the multinode pacemaker technology due to the size constraints of the capsule antenna. These kinds of WPT techniques can be categorized as interference-based WPT, which includes EM radiation and multipath propagation. Adaptive focusing technologies for the wireless powering of implanted devices have recently been reported [21], [22]. By performing the phase-conjugated operation on the incident signal (transmitted by Rx) and then transferring the signal back to the source, coherent RF power can be achieved at the Rx. This has been shown to improve WPT efficiency.

Although several studies on improving WPT efficiency have been reported, these studies show a lack of systematic consideration of WPT scenarios [27]. The entire typical WPT process is clearly demonstrated in Fig. 1(a). When EM waves propagate from air into biological tissue, the reflection at the interface of air and biological tissue, and the attenuation in biological tissue appear in sequence, resulting in high propagation loss. This has been shown to severely reduce the efficiency of the WPT. Therefore, the key challenge in designing an efficient WPT system for application to implantable devices is to reduce propagation loss. In other words, reflection and attenuation should be analyzed simultaneously.

Near-field-focused (NFF) antenna can focus the EM field at a point in the antenna near-field region that determines an increase in the EM power density in a size-limited region close to the antenna aperture [28], [29], [30], [31]. The Fresnel zone plate (FZP) lens has been considered to implement the NFF

planar lens antenna, which has the benefit of being lighter and easier to design and manufacture compared to the traditional NFF antenna, such as array antennas and reflectarrays. However, the traditional design theory cannot directly design the FZP applied to biological tissue due to the different media of the application scenarios. Therefore, a design method for FZP considering the characteristics of biological tissues is required.

Impedance matching is a fundamental concept in EM theory that can eliminate the reflection at the interface. A lot of work has been reported recently using a matching layer (ML) or metasurface/metamaterial to improve the efficiency of WPT. However, the following problems still exist: the operating principles are not clearly explained, and the used matching layer is limited by available thickness and substrate [23], [32]. This indicates that a practically available and specially designed matching layer is required for biological tissue WPT applications, in which the operating mechanism can be clearly explained by classical theory. As recently reported in [33], a new matching technology named artificial ML (AML) is proposed that can design matching layer by substrates with arbitrary permittivity even though the limitation of the thickness of substates still makes matching impractical.

A systematic method for efficient wireless powering to implantable medical devices and the design principle are presented in Fig. 1(b) and (c). The method is based on an analysis of the two main causes of high propagation loss: in-tissue attenuation and interface reflection. To decrease the propagation loss and comprehensively improve the WPT efficiency, on the one hand, we improve the traditional FZP design method by considering permittivity change in different areas and propose FZP for in-tissue energy focusing against the in-tissue attenuation; on the other hand, we propose a novel matching technology named air layer-AML (AL-AML) to decrease the interface reflection by introducing air layer into the design of AML to break the limitation of using substrates with restricted thickness and make matching with biological tissue feasible. The efficiency of this WPT with a combined FZP and AM-AML system was determined and then applied to an implantable biomedical device for verification. To the best of our knowledge, this is the first time a systematic method instead of existing single methods is proposed to realize an efficient WPT system applied to biomedical devices.

This article is organized as follows. In Section II, the systematic methods and corresponding solutions are introduced along with the design process of the proposed FZP and AL-AML. In Section III, an analysis and a discussion of the four models are presented to clearly demonstrate the performance of the proposed systematic method. In Section IV, experiments are performed to verify the effectiveness of the proposed methods. Finally, a brief conclusion of this work is drawn in Section V.

II. DESIGN METHODS AND PROCESS

A 2.45 GHz operation frequency, which is within the Industrial Scientific Medical Band (ISMB), was chosen for this design. While the operation frequency is not considered critical in the design, the advantages of operating at a higher frequency on miniaturization make it essential in the design of implanted
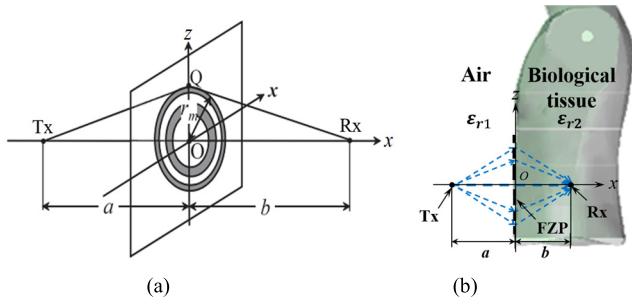
Fig. 2. Process of designing an FZP applied to in-tissue focusing. (a) Fundamental structure of an FZP. (b) Application scenario of the proposed FZP.

Fig. 3. Normalized E-field magnitude distribution along the x-axis for a different number of zone plates.

devices. Also, smaller wavelengths at higher frequencies allow more precise control in the distribution of EM waves so that critical organs can be avoided. Besides, the smaller wavelength makes a larger electrical size for a fixed physical size, which is necessary for the design of lenses and metasurfaces for obtaining better performance, according to the antenna theory.

A. Consideration of Biological Tissue

Biological tissue is a kind of lossy media with electrical characteristics that change with frequency. Different liquid mixtures of sugar, salt, organic compound solution, and deionized water have been used to simulate biological tissue in studies [16], [34]. However, comparing biological tissue to other mediums inevitably leads to inaccuracies. The human body equivalent liquids (HBEL, MBBL-1900-3800V3) produced by Schmid & Partner Engineering AG (SPEAG) is a liquid with dielectric parameters that simulate the body-tissue parameters defined in the specific absorption rate (SAR) measurement guide [35]. The dielectric parameters of HBEL are matched to the target tissue parameters over a certain frequency range. For accurate comparison and discussion, HBEL is used to imitate biological tissue (muscle) in both simulation analysis and experiments in this work.

B. Fresnel Zone Plate Applied Against Attenuation of Biological Tissue

When EM waves propagate inner biological tissue, large attenuation will appear, and the WPT efficiency will be reduced due to the high conductivity of biological tissue. Therefore, one of the methods to increase WPT efficiency is to decrease the extent of attenuation.

The FZP consists of a set of radially symmetric opaque and transparent rings. When the EM waves encounter the zone plate, they diffract around the opaque zones, causing the cophase components to interfere at the desired focal point and create high field density. Since their invention, FZPs have been used to focus energy as a lens at optical and microwave frequencies [36]. Fig. 2(a) shows the fundamental structure of the FZP. Parameter a is the source point distance, which is defined as the distance between the Tx and the FZP. Parameter b is the focal point distance, which is defined as the distance between the Rx and the FZP. λ_0 is the free-space wavelength at 2.45 GHz. The radius r_m of each Fresnel zone can be
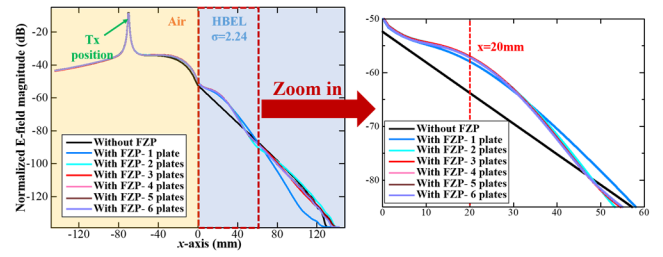
calculated using the following equation [37]:

$$\sqrt{a^2 + r_m^2} + \sqrt{b^2 + r_m^2} - (a + b) = \frac{m\lambda_0}{2}, \quad m = 1, 2, 3, \ldots \quad (1)$$

The focusing property of FZP can be used to accumulate energy in biological tissue against the attenuation of EM waves. However, (1) is no longer useful in this application. It can be seen from (1) that the design of the FZP in free space is only related to the wave path difference. In this work, the two sides of the FZP are air and biological tissue, respectively, as shown in Fig. 2(b). It should be noted that the characteristics of the two media are totally different. There, it is necessary to design an FZP with effective focusing characteristics between different media.

The principle of focusing is cophase superposition. It must be noted, however, that the influence of biological tissue is the wavelength change of the EM waves, which occurs largely due to high permittivity. That is, in order to focus energy, the wave phases of different paths at desired focal point are required to be the same regardless of the changes in the wavelength. Therefore, assuming that the relative permittivity of media on both sides are ε_{r1} and ε_{r2}, by considering the influence of permittivity and in cophase superposition point of view, the design equation of FZP can be amended to the following equation:

$$\sqrt{\varepsilon_{r1}} \cdot \sqrt{a^2 + r_m^2} + \sqrt{\varepsilon_{r2}} \cdot \sqrt{b^2 + r_m^2} - \left(\sqrt{\varepsilon_{r1}} \cdot a + \sqrt{\varepsilon_{r2}} \cdot b\right)$$
$$= \frac{m\lambda_0}{2}, \quad m = 1, 2, 3, \ldots \quad (2)$$

By inputting ε_{r1} and ε_{r2} and selecting proper a and b according to the condition of the WPT environment, the effective FZP can be designed. Note that the number of zone plates is a key parameter that determines the focusing effect and should be properly chosen according to the actual application. Fig. 3 shows the normalized electric field (E-field) magnitude versus the x-axis value for different numbers of zone plates. Note that the Tx is a dipole antenna and the Rx is omitted in this simulation to clearly observe the E-field distribution at the focal point. It can be seen that, when the number of zone plates increases from 1 to 3, the normalized E-field magnitude around the focusing point will be increased significantly. It is indicated that the number of zone plates should be greater than or equal to 3 to obtain a significant focusing effect. However, when the number of zone plates continues to increase over 3, the E-field magnitude will be not further focused anymore. This
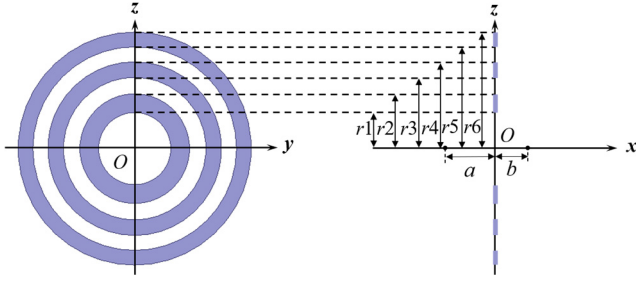
Fig. 4. Structure of the proposed FZP.

TABLE I
PARAMETERS OF THE PROPOSED FZP

Parameter	Value	Parameter	Value
ε_{r1}	1	$r2$	30.9 mm
ε_{r2}	47.2	$r3$	40.5 mm
a	70 mm	$r4$	49.5 mm
b	20 mm	$r5$	58.2 mm
$r1$	20.3 mm	$r6$	66.7 mm

is because the illumination efficiency of the FZP decreases as the number of zone plates increases. The huge loss inside the HBEL also reduces the contributions of the zone plates placed at a distance. It was found that a larger number of zone plates do not result in a significant improvement in the focusing effect: it only increases the system volume. Therefore, three zone plates are included in the design of the FZP, as shown in Fig. 4. All design parameters are listed in Table I. The simulation results and discussion are given in Section III.

C. Air Layer-Artificial Matching Layer Applied to Reducing Reflection of Biological Tissue

Another reason for generating propagation loss that causes the deterioration of WPT efficiency is the interface reflection when EM wave propagates from air to biological tissue of high permittivity. An matching layer is a basic concept and an example of impedance matching technologies in EM theory. By choosing the proper permittivity and thickness of the substrate of matching layer, the interface reflection can be eliminated. According to the EM theory, the relative permittivity ε_{r3} and thickness d can be calculated using the following equation [38]:

$$\varepsilon_{r3} = \sqrt{\varepsilon_{r1}\varepsilon_{r2}}$$
$$d = \frac{1}{4}(2n + 1)\lambda_3, \quad n = 0, 1, 2, \ldots \quad (3)$$

where ε_{r1} and ε_{r2} refer to the relative permittivities of medium 1 and medium 2, respectively, and λ_3 is the wavelength in the matching layer. The permittivity and the thickness of the matching layer are determined by medium 1 and medium 2. For this reason, it is almost impossible to realize matching by the limited materials suitable for use in this type of device.

Recently, a kind of matching technology referred to as AML was reported by Yang et al. [33]. By introducing a metasurface into the matching analysis, an matching layer using arbitrary permittivity is achieved. However, the fixed
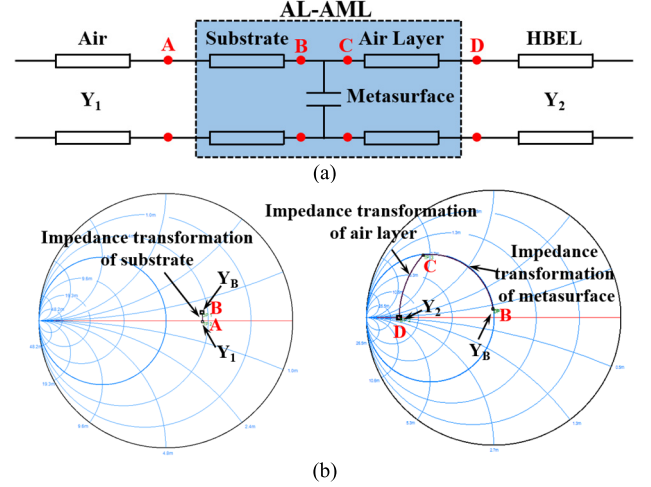

Fig. 5. Matching mechanism of the AL-AML. (a) Equivalent transmission line model. (b) Matching process using the Smith chart.

thickness of the substrate is still a limitation in AML design, which makes it impractical in applications. To solve this problem, in this investigation, we propose a novel practical matching technology, which can be applied to the surface matching of biological tissue. This design, which we refer to as the AL-AML, introduces an air layer into the design of the AML. The problem posed by a substrate with restricted thickness is solved by transferring the requirement of thickness from the substrate to the air layer. In this way, matching layers with substrates of arbitrary permittivity and thickness can be designed.

To illustrate the matching mechanism of the AL-AML, an equivalent transmission line model is drawn in Fig. 5(a). The air and the biological tissue are represented with different characteristic admittances by the following equation:

$$Y_i = \sqrt{\varepsilon_i/\mu_i}, \quad i = 1, 2 \quad (4)$$

where ε_i and μ_i are the permittivities and permeabilities of corresponding media, respectively. AL-AML is inserted between the air and the biological tissue to achieve total transmission. The proposed AL-AML consists of three parts: the substrate, the metasurface (capacitive), and an air layer. When an arbitrary substrate is given, impedance matching will be achieved by the use of a proper metasurface and an air layer. The determinations of susceptance of the metasurface (B_{MS}) and thickness of the air layer are discussed below. Four key points A, B, C, and D with characteristic admittances of Y_A, Y_B, Y_C, and Y_D are also marked. Note that Y_A is equal to Y_1, and Y_D is equal to Y_2.

The matching procedure in the Smith charts is also plotted in Fig. 5(b) for a clear demonstration. First, Y_A and Y_D are given. Y_A is the susceptance at the left-hand side (source side) of the substrate, and Y_B is the susceptance at the other side (load side). Since the substrate can be regarded as a segment of a lossless transmission line, Y_B can be obtained by the anticlockwise moving of Y_A along the equal standing-wave ratio (SWR) circle with a certain electric length of transmission line in the Smith chart. The electric length can be calculated when the permittivity and thickness of the substrate

TABLE II
PARAMETERS IN THE DESIGN PROCESS OF THE PROPOSED AL-AML

Parameter	Value	Parameter	Value
Y_A	2.6×10^{-3} S	Y_D	1.8×10^{-2} S
Y_B	$(2.7 - j0.4) \times 10^{-3}$ S	B_{MS}	$j5.6 \times 10^{-3}$ S
Y_C	$(2.7 - j5.9) \times 10^{-3}$ S		

are given. After determining Y_B, the next step is to make Y_D equal to Y_B through the metasurface and the air layer. The air layer can also be regarded as a segment of a lossless transmission line; therefore, Y_C can be obtained by clockwise moving Y_D along the equal SWR circle while considering the relative location of Y_C and Y_D. On the other hand, because the metasurface can be regarded as a shunt susceptance, Y_C can be obtained by moving Y_B anticlockwise along the equal conductance circle while considering the relative location of Y_C and Y_B. The point of intersection between the equal SWR circle and the equal conductance circle is the position of Y_C. The susceptance value of the metasurface is determined by the susceptance at point C. The air layer thickness d is determined by the path length from point C to point D. In this work, we use polyphenylene ether (PPE) as the substrate with a permittivity of 3.3 and a thickness of 1.2 mm. Through the analysis above, the desired susceptance of the metasurface and the thickness of air layer are 0.0056 S and 7.06 mm, respectively. The related parameters of the design process are summarized in Table II.

In summary, the matching procedure is similar to a single stub shunt tuning circuit surrounded by two segments of the transmission line with different characteristic admittances in the transmission line theory. More importantly, the air layer is introduced to act as a segment of "substrate." As a result, the AL-AML can use arbitrary substrates, which is no longer limited by available substrates with specific permittivity and thickness.

After analyzing the circuit model, the next step is to design a metasurface with a required susceptance. Various metallic shapes (dipoles, crosses, patches, etc.) can be used to design the metasurface, and a square loop is chosen here due to its simplicity and its capability to achieve both capacitive and inductive susceptances. The configuration of the AL-AML unit is shown in Fig. 6(a). It can be seen that the AL-AML consists of a substrate, a metasurface, and an air layer, respectively. The metasurface is printed at the bottom of the substrate, and the air layer is inserted between the metasurface and HBEL. The design frequency is set at 2.45 GHz. In Fig. 6(a), rl is unit periodicity, t is the thickness of the given substrate, and d is the thickness of air layer determined in the aforementioned steps. ro and rs are the side length and width of the metallic square loop, respectively. When t and d are given, the equivalent susceptance can be achieved by selecting proper rl, ro, and rs. The parameter values of the AL-AML unit are given in Table III.

For use in verifying the design, the equivalent transmission line model and the unit model discussed above are calculated in an advanced design system (ADS) and a full-wave simulator high-frequency structure simulator (HFSS), respectively.
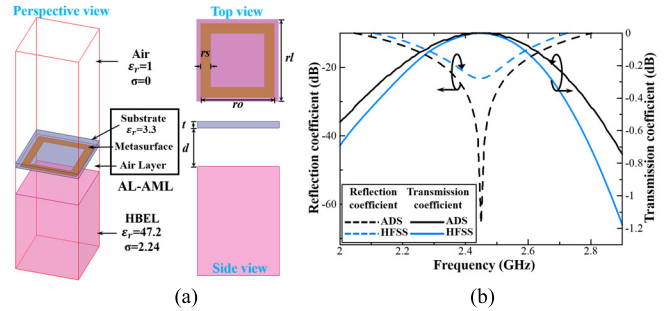

Fig. 6. Proposed AL-AML unit. (a) Configuration of the designed AL-AML unit. (b) Simulated S-parameter results.

TABLE III
PARAMETERS OF THE PROPOSED AL-AML UNIT

Parameter	Value [mm]	Parameter	Value [mm]
ro	13.5	t	1.2
rs	3.6	d	7.06
rl	15		

Specifically, the simulation in HFSS is performed under the Floquet ports and periodic boundary conditions. The simulated S-parameters are plotted in Fig. 6(b). It can be seen from the $|S_{11}|$ curve that the minimum value of reflection is 2.45 GHz, and $|S_{21}|$ reaches a maximum value of 0 dB. This is evidence that all the energy has passed through at 2.45 GHz. The results fully show that the interface matching has been achieved by the proposed AL-AML. Note that the slight difference between ADS and HFSS results is mainly due to the roughly simplifying the actual E-field distribution to TEM wave and property setting of HBEL at only a fixed frequency point in ADS.

Finally, the proposed efficient WPT system is obtained by integrating the designed FZP and AL-AML with a conventional WPT system, which only contains an out-tissue Tx and an in-tissue Rx. The performance of the proposed WPT system is discussed in the following. Note that, although the proposed FZP and AL-AML are individually designed, the simulated and experimental results discussed in Section III show that they are not only insusceptible to each other but also mutually reinforce the performance of the system.

III. SIMULATION ANALYSIS

A. Simulation Model

Fig. 7(a) shows the structure of the proposed efficient WPT system. The proposed WPT system contains five parts: Tx, Rx, HBEL, FZP, and AL-AML. Here, biological tissue is modeled as a tank filled with HBEL. The length and width of the tank are both L, and the thickness is H. The FZP is placed at the interface of the air and HBEL. Tx is placed at the source point of FZP in the air region, and Rx is placed at the focusing point of FZP in the HBEL region. The distances from Tx and Rx to the FZP are a and b, respectively. The AL-AML substrate is placed before FZP at a distance of d, which is also the thickness of the air layer. The metasurface is printed at the
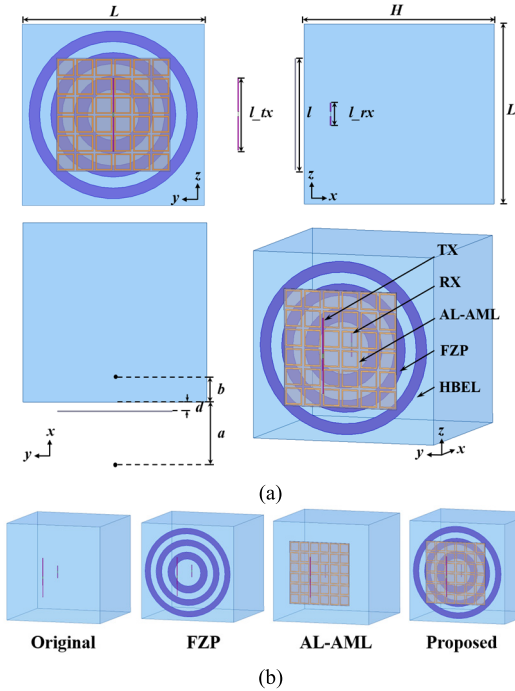
Fig. 7. Simulation model in SEMCAD. (a) Structure of the proposed WPT system. (b) Four simulated models.

TABLE IV
PARAMETERS OF THE PROPOSED WPT SYSTEM

Parameter	Value [mm]	Parameter	Value [mm]
L	144	l	90
H	144	a	70
l_tx	58	b	20
l_rx	18	d	7.06

bottom layer of the substrate. The centers of Tx, Rx, FZP, and AL-AML are collinear.

To reduce the complexity of the system and clearly demonstrate the operating principle, dipole antennas are used as Tx and Rx in this work. The lengths of Tx and Rx are l_tx and l_rx. Note that, even though the adoption of other types of well-designed high-gain antennas may further increase the system performance, the effectiveness validation of the proposed systematic method is the focus of this investigation. For this reason, fundamental dipole antennas are used in this article, and no realistic electronics are connected to Rx. All of the parameters of the proposed WPT system are listed in Table IV.

All simulations in this section are calculated via commercial software SEMCAD X by SPEAG based on the finite-difference time-domain (FDTD) method. In order to clearly verify the effect of the proposed methods, calculations were made for the four models shown in Fig. 7(b): Model 1, denoted as "Original," is the original WPT system with only Tx and Rx; Model 2, denoted as "FZP," is the "Original" model plus designed FZP; Model 3, denoted as "AL-AML," is the "Original" model plus designed AL-AML; and Model 4, denoted as "Proposed," is the "Original" model integrated with a combined FZP and AL-AML approach.
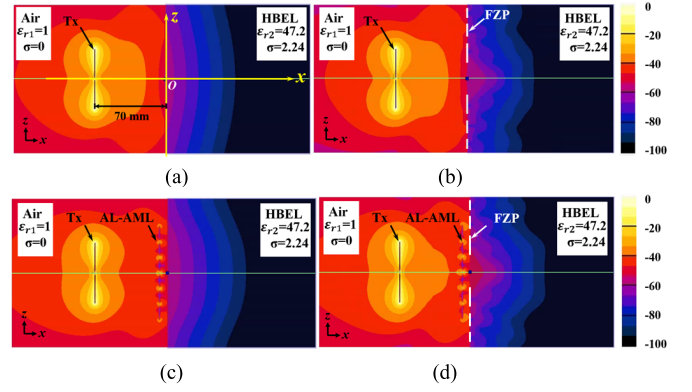

Fig. 8. Normalized E-field magnitude distribution in the *xoz* plane. (a) Original. (b) FZP. (c) AL-AML. (d) Proposed.
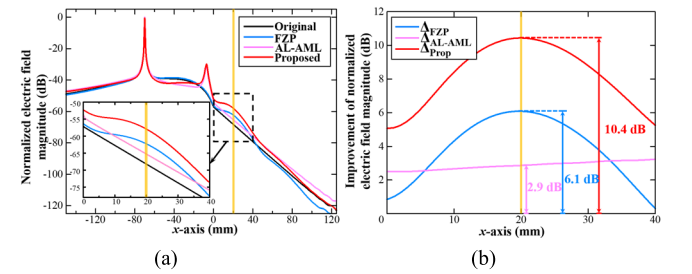

Fig. 9. Normalized E-field magnitude distribution along the *x*-axis. (a) Curve of the normalized E-field magnitude versus the *x*-axis. (b) Improvement of the normalized E-field magnitude.

B. E-Field Distribution

The E-field distribution is simulated to intuitively illustrate the operating principle and effect of the proposed structures. Fig. 8 shows the E-field magnitude distribution in the *xoz* plane. Note that Rx is removed in this simulation to clearly show the E-field distribution. Fig. 8(a) shows that the E-field, generated by Tx, is distributed throughout the air region and attenuates significantly and uniformly in the HBEL region due to the high propagation loss caused by biological tissue. It can be seen from Fig. 8(b) that the E-field is mainly distributed in the central part of the HBEL region and the magnitude increased significantly. The interference pattern, which appears in the HBEL region, is characteristic of the lens and, therefore, verifies the effect of FZP. As shown in Fig. 8(c), the E-field increased uniformly in the HBEL region by using AL-AML, which is the characteristic of the matching layer. The E-field distribution in Fig. 8(d) can be regarded as the combination of the two cases mentioned above. The E-field distribution in Fig. 8(d) is the result of the combination of the two cases mentioned above. The interference pattern becomes more obvious, and the E-field magnitude is increased further.

Fig. 9(a) shows the curves of normalized E-field magnitude versus the *x*-axis. The peak appears at −70 mm where Tx is placed. It can be seen that, in the $x \geq 0$ mm region (HBEL region), the E-fields attenuate with different degrees and differ clearly in the $0 \leq x \leq 40$ mm region. In this region, the AL-AML has the same degree of attenuation as the Original but a higher value of magnitude, indicating that the magnitude
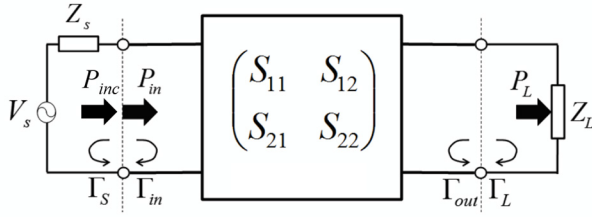
Fig. 10.   Two-port network equivalent circuit applied to WPT.

of the E-field increases uniformly in the AL-AML. The curves for the FZP and the Proposed have the same tendency: the hump at around $x = 20$ mm indicates that the energy increased sharply and became focused around the designed position.

The Δ curve in Fig. 9(b) clearly shows the effect of FZP, AL-AML, and the proposed system. We define the Δ curve as the difference in values between each system and the original system, which are denoted as Δ_{FZP}, $\Delta_{\text{AL-AML}}$, and Δ_{Prop}. A stable increment of about 3 dB is achieved by using AL-AML, which reflects the characteristic of the matching layer. In the curves for the FZP and Proposed, the curves first increase before decreasing. The peak values appear at $x = 20$ mm, which is the designed focal point. These kinds of growth trends show the focusing characteristic of FZP. The peak incremental values of the FZP and Proposed are 6.1 and 10.4 dB, respectively. As discussed in the result discussion part of Section IV, a large amount of enhancement of the E-field leads to significant improvement in the WPT efficiency. Moreover, it can be found that the improvement provided by the Proposed is larger than the sum of FZP and AL-AML. This is evidence of the superiority of the systematic method over traditional single methods. This characteristic is discussed in detail in Section IV.

C. Transmission Factor

In most existing WPT research, in addition to the WPT efficiency, the transmission coefficient ($|S_{21}|$) is also used to evaluate the relative received power. However, in our previous studies, we concluded that greater attention should be given to propagation loss than to the transmission coefficient because the mismatch of antenna ports can be resolved by circuit-matching technologies [39], [40]. Therefore, the transmission factor τ is used as an indicator of propagation loss in this work. The two-port network equivalent circuit applied to WPT is shown in Fig. 10. Transmitting antenna is connected to a source with an internal impedance of Z_S, while receiving antenna is loaded with an internal impedance of Z_L. P_L is the power delivered to the load Z_L, P_{inc} is the incident power, P_{in} is the input power, and Γ_S and Γ_L are the reflection coefficients looking toward the source Z_S and the load Z_L, respectively. The transmission factor τ is the relative maximum received power under the condition that the complex-conjugate matching conditions are satisfied at both transmitting and receiving ports, and is defined using S-parameters by the following equation [41], [42]:

$$\tau = \frac{P_L}{P_{\text{inc}}}\bigg|_{Z_s=Z_{in}^*, Z_L=Z_{out}^*} = \frac{P_L}{P_{\text{in}}} = \frac{1}{1-\left|\Gamma_s\right|^2}\left|S_{21}\right|^2\frac{1-\left|\Gamma_L\right|^2}{\left|1-S_{22}\Gamma_L\right|^2}. \tag{5}$$
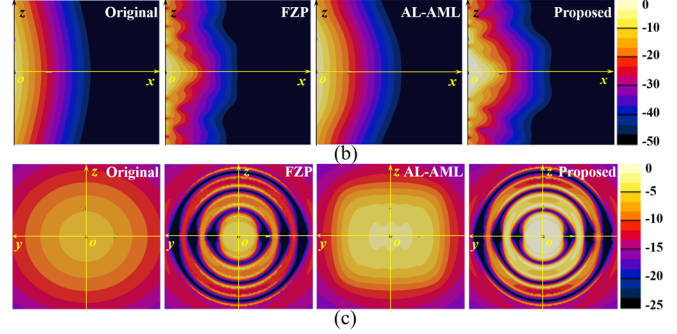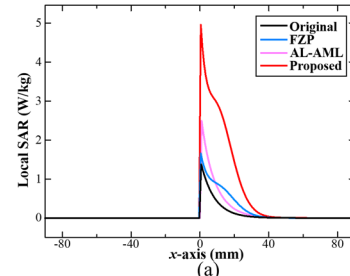

Fig. 11.   Simulated local SAR distribution. (a) SAR distribution along the x-axis. (b) SAR distribution in the xoz plane (only shows the HBEL region). (c) SAR distribution in the yoz plane.

In order to avoid redundancy, the simulated results of the transmission factor are given in Section IV together with the measured ones (as shown in Fig. 17). Also, the transmission coefficients are also plotted to allow comparison with the results of earlier studies (as shown in Fig. 16).

D. Specific Absorption Rate

The SAR is an important index used to describe the influence of EM waves on biological tissue. In a given region, the SAR is computed as the ratio between the dissipated power and the mass densities. This is denoted as local SAR and is described by the following equation:

$$\text{SAR}(\boldsymbol{r}) = \frac{\sigma}{2\rho}E^2 \propto \frac{dT}{dt} \tag{6}$$

where $E^2 = \boldsymbol{E} \cdot \boldsymbol{E}^*$ denotes the squared magnitude of the induced E-field, $\rho \equiv \rho(\boldsymbol{r})$ is the mass density (kg/m^3), and T is the temperature (K).

Usually, SAR is mostly presented in an averaged form over the region mass as follows:

$$\langle\text{SAR}\rangle_M = \frac{1}{M}\int_{R(M)}\text{SAR}(\boldsymbol{r})\,dm \tag{7}$$

where $M = \int_{R(M)}\rho\,dv$ is the mass of the integration region R.

The simulated local SAR distribution is shown in Fig. 11. The input power is set as 1 W in all simulations. For quantitative analysis, the SAR distribution curve on the x-axis is plotted in Fig. 11(a). It is observed that the SAR is mainly distributed near the interface of air and HBEL on the HBEL side. The peaks of local SAR occur at the interface with the values of 1.38, 3.53, 2.49, and 4.95 W/kg, respectively. In addition, the 2-D local SAR distributions in the xoz plane
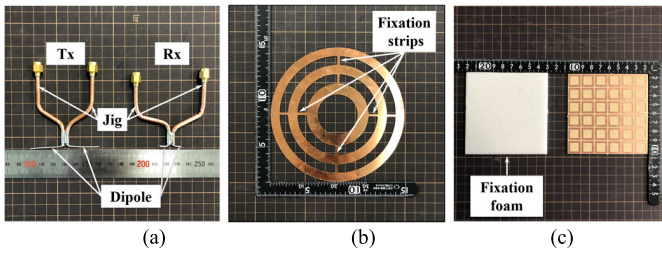
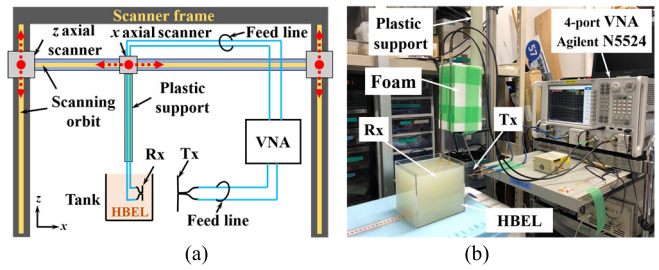Fig. 12. Fabrication photographs. (a) Tx and Rx. (b) FZP. (c) AL-AML.

Fig. 13. Experimental setting. (a) Schematic of the experimental equipment. (b) Experimental environment.
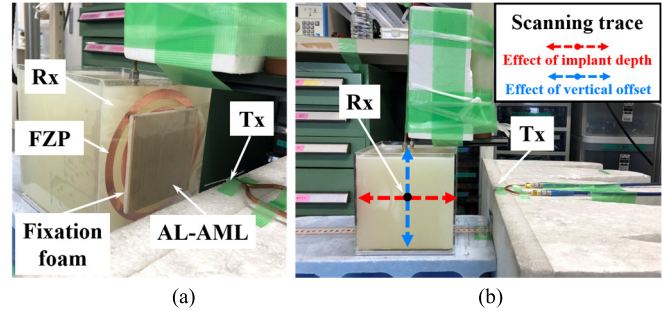

Fig. 14. Measurement photographs. (a) Transmission coefficient measurement. (b) Measurement of influences of the implant depth and the vertical offset.

and the *yoz* plane are plotted in Fig. 11(b) and (c). Note that all the SAR values are normalized to 4.95 W/kg for easy comparison. It can be found that the SAR of the proposed system is mainly distributed in the designed first three Fresnel zones and has a larger and deeper distribution region. Moreover, the psSAR (maximum SAR averaged over 10 g tissue) was also calculated. The psSARs of Original, FZP, and AL-AML are 0.48, 0.8, and 0.9 W/kg, respectively. All of these values are far below the IEEE standard of psSAR limitation of 2 W/kg [43]. In addition, the psSAR of the proposed system is 2.43 W/kg, which is slightly beyond the standard limit. Therefore, careful measures, such as decreasing the input power of Tx, should be employed in practical applications for safety considerations.

IV. EXPERIMENT AND RESULTS

A. Fabrication and Setting of Experiment

Fig. 12 shows the photos of fabricated Tx, Rx, FZP, and AL-AML. The fabricated Tx and Rx dipole antennas are shown in Fig. 12(a). Note that the S-parameter method is used in experiments, which is a wideband balanced feeding method especially suited to feed antennas under water or liquids. Therefore, each dipole antenna is connected with two ports by a jig segment as the S-parameter method's requirement [44], [45]. Fig. 12(b) shows the fabricated FZP. Note that four fixation strips with a width of 2 mm are made to fix the relative position of the three plates. It has been verified by simulation that the addition of fixation strips has little impact on the results (0.2 dB difference in transmission coefficient). Fig. 12(c) shows the fabricated AL-AML. The substrate material is CS-3376C produced by RISHO KOGYO CO., LTD. with a relative permittivity of 3.3 and a loss tangent of 0.004 at 2.45 GHz. The thickness of the substrate is 1.2 mm, and the metasurface is printed at the bottom layer of the substrate. Moreover, a foam with relative permittivity of around 1 and the same size as AL-AML is also fabricated to fix the position of AL-AML in the experiment.

The experimental setup, as shown in Fig. 13(a), consists of the following parts: four-port VNA (Agilent N5524A), planar scanner, scanning orbit, plastic support, Tx and Rx antennas, and HBEL. Plastic support is used to fix Rx and connect Rx with the scanning orbit controlled by the planar scanner. Therefore, Rx can scan to any point on the vertical plane by inputting the position information into the planar scanner. A detailed photograph of the experimental environment is provided in Fig. 13(b). The settings of the experiment are

given as follows: Tx and Rx are, respectively, connected with four-port VNA by feed lines. The output power of VNA is 0 dBm. Tx is fixed to the outside of the HBEL at a distance of 70 mm from the surface, and Rx is implanted inner HBEL. Here, HBEL is contained in a plastic tank with a relative permittivity of 2.2 and a thickness of 3 mm. The influence of the tank was considered in the simulation, which is very small and can be neglected. The FZP is fixed at the inner surface of the tank, while the AL-AML is fixed at the other side of the tank by a piece of foam. The total thickness between FZP and AL-AML is 7.06 mm. In the experiment of measuring transmission coefficient and transmission factor, Rx is fixed inner HBEL at a distance of 20 mm. In the experiment of measuring the effect of implant depth and vertical offset, Rx is controlled to move along the scan trace by the planar scanner. The photographs of measurement are shown in Fig. 14. The parameters of the experiment are the same as those in the simulation model, which have been given in Table IV. Note that each experiment is conducted four times for comparing the effects of the four models.

B. Results and Discussion

It can be seen from the measured and simulated reflection coefficients of the four models in Fig. 15 that the simulated and measured $|S_{11}|$ are in good agreement. Second, both the simulated and measured results almost remain unchanged for the four models, which indicates the good compatibility of the proposed system. In terms of $|S_{22}|$, the measured results of the four models are in good agreement. Meanwhile, the resonance of simulated results will shift to a higher frequency when the FZP is adopted. The discrepancy between the simulated and measured results is mainly due to the simplified simulation
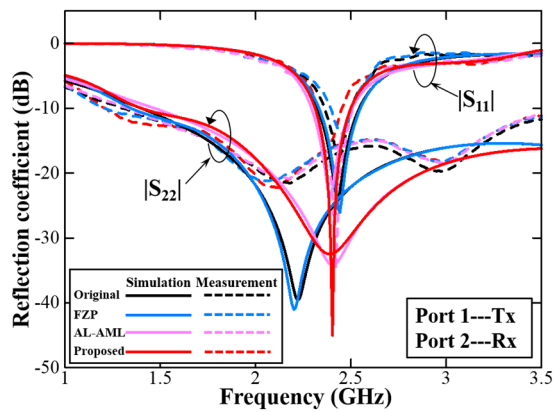
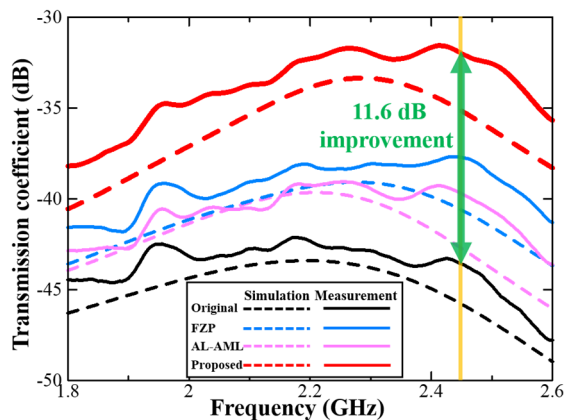Fig. 15. Measured and simulated reflection coefficients.

Fig. 16. Measured and simulated transmission coefficients.

TABLE V
MEASURED TRANSMISSION COEFFICIENT VALUES AT 2.45 GHz AND COMPARISON WITH SIMULATION RESULTS

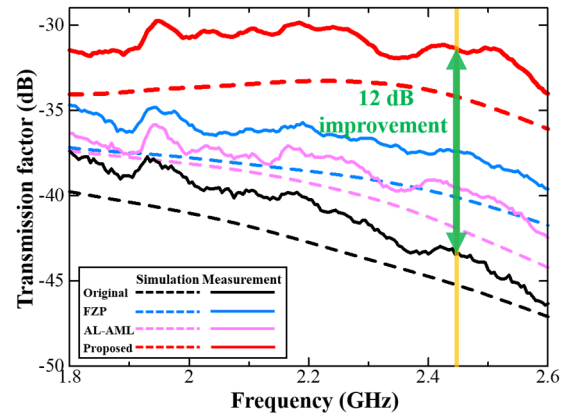| Transmission Coefficient	Experiment [dB]	Simulation [dB]
Original	-43.6	-45.8
FZP	-37.7	-40.6
AL-AML	-39.7	-42.7
Proposed	-32	-35.2
Δ_{FZP}	5.9	5.2
Δ_{AL-AML}	3.9	3.1
Δ_{Prop}	11.6	10.6

Fig. 17. Measured and simulated transmission factors.

TABLE VI
MEASURED TRANSMISSION FACTOR VALUES AT 2.45 GHz AND COMPARISON WITH SIMULATION RESULTS

Transmission Factor	Experiment [dB]	Simulation [dB]
Original	-43.4	-45.3
FZP	-37.4	-40.1
AL-AML	-39.5	-42
Proposed	-31.4	-34.2
Δ_{FZP}	6	5.2
Δ_{AL-AML}	3.9	3.3
Δ_{Prop}	12	11.1

models of Tx and Rx, which do not consider the influence of the jig and the effect between the jig and HBEL. Note that all the reflection coefficients are below −10 dB within the operating frequency, which is evidence of the good matching characteristics of Tx and Rx.

Fig. 16 shows the measured and simulated transmission coefficient results. The good agreement between the measured and simulated curves verifies the design theory. All of the curves increased at first, reaching a peak value of around 2.45 GHz, and then decreased. Table V lists the measured transmission coefficient values at 2.45 GHz and provides a comparison with simulated results. The increments of transmission coefficient obtained by using FZP and AL-AML were 5.9 and 3.9 dB, respectively. Most importantly, an enhancement in the measured transmission coefficient of 11.6 dB by the proposed system was observed, with the received power improved by a factor of 14.45 compared with the original system.

To further evaluate the WPT efficiency, the transmission factors were measured. The measured results have the same tendency as the simulated results, as can be seen in Fig. 17. It should be noted that the stable differences of 2–3 dB between the measured values and simulation results in Figs. 16 and 17 can mainly be attributed to the characteristic changes (decrease of permittivity or conductivity) of HBEL

due to prolonged storage and environmental changes [46]. In addition, the RF leaks within the operating frequency band from free space would also affect measured results. The transmission factor values at 2.45 GHz are also given in Table VI with the simulated results. It was observed that 6, 3.9, and 12 dB increments of the transmission coefficient are obtained by using FZP, AL-AML, and the proposed system, respectively. The increase in the relative maximum received power was 15.8 times greater than that in the original system. This is clear evidence of the improved efficiency of the proposed WPT system. It should also be noted that both the simulated and measured transmission factors are almost the same as the transmission coefficients. In other words, the matching loss is very slight in this work, and the measured received power is very close to the theoretical upper limit.

The proposed systematic method not only greatly improves the WPT efficiency but also shows the superiority of the
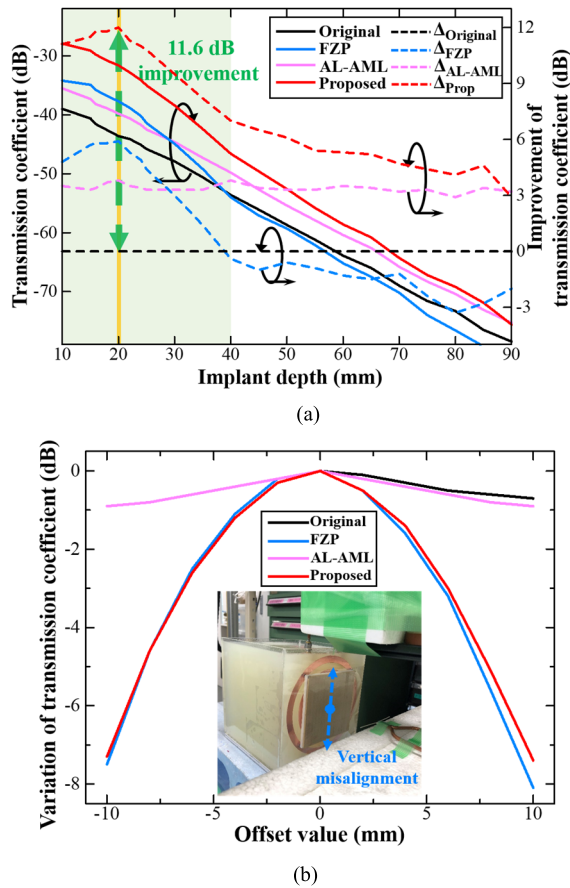
(a)

(b)

Fig. 18. Effect of implant depth and vertical offset of Rx. (a) Measured change and improvement of transmission coefficients along with the implant depth. (b) Effect of the vertical translation offset misalignment of Rx.

proposed systematic method over other ordinary methods. In both the simulated and experimental results listed in Tables V and VI, Δ_{Prop} is larger than Δ_{FZP} plus Δ_{AL-AML}. In other words, the improvement of using FZP and AL-AML simultaneously is better than the sum of the improvement of using FZP and AL-AML, respectively, which means that FZP and AL-AML are mutually reinforcing. The reason for this phenomenon is that the main contribution to the focusing characteristic of the designed FZP is the E-field within the first Fresnel zone, where it is significantly further enhanced by the existence of AL-AML. This allows the total effect to be further improved. However, in other studies, only the antenna configuration is typically modified to increase transferred power, like in the FZP used in this article, which leads to a limited effect on improving WPT efficiency. The results of this investigation show that the systematic method has the characteristic of "1 + 1 > 2" and reveals the superiority of the proposed systematic method over single methods.

To clearly understand how the proposed structures would help the WPT efficiency, the measured transmission coefficients of the four models, as a function of implant depth, are shown in Fig. 18(a) for the purpose of comparison (in solid line). The same trends as the curves shown in Fig. 9(a) are observed, verifying the analysis of the operating principle of each component in Section III. Moreover, the corresponding Δ curves are also plotted in Fig. 18(a) (in dashed line). The

main increase in the transmission coefficient is around the design implant depth of 20 mm (green zone in the figure). The measured largest increment of 11.6 dB is also obtained at this position. This focused transmission coefficient distribution not only ensures the improvement of WPT efficiency but also reduces the impact of the increased transferred power on other nontarget organs or tissues. Furthermore, the measured results shown in Fig. 18(a) agree well with the simulated results shown in Fig. 9, indicating the correctness of the proposed design theories.

In practical applications, the FZP and AL-AML are likely to be wearable devices. That is, they would be combined with clothing or medical adhesive tape, which may inadvertently result in a misalignment between the FZP or AL-AML and the implanted Rx element. Therefore, it is necessary to discuss the influence of misalignment tolerance. To simplify the analysis process, the position of Rx is changed in the experiment to simulate misalignment. Therefore, it is necessary to discuss the influence of misalignment tolerance. To simplify the analysis process, the position of Rx is changed in the experiment to simulate misalignment. Fig. 18(b) shows the effect of the vertical translation offset misalignment of Rx. The transmission coefficient decreases as the offset value becomes larger in all cases. As for original and AL-AML systems, the effect of vertical translation offset is slight because the energy distribution is almost uniform in the vertical direction. However, the effect of translation offset is significant due to the focusing characteristic in the FZP and proposed systems. When the offset value is 5 mm, the received power is only half that of the normal situation. That is to say, the position of implanted Rx should be strictly fixed for excellent performance when using FZP in practical applications. We recommend that the maximum absolute offset value should not exceed 3 mm, which would allow receiving at least 80% of the maximum power, while the limits can be extended to 10 mm if only AL-AML is used in the actual application.

Table VII shows the results for the proposed WPT system with the results of previous works. Some necessary parameters and information related to transfer efficiency are given for the purposes of a clear comparison, including operating frequency, antenna types of Tx and Rx, transfer distance, and implant distance. Here, we put the emphasis on just two parameters for comparison: the implant distance and the transmission coefficient ($|S_{21}|$). In the study by Bose et al. [20], only the WPT performance over a long distance was evaluated, and no measure to improve WPT efficiency was reported. The results of this investigation, however, showed a remarkable improvement in efficiency (represented by $|S_{21}|$ and τ), especially over long working distances (both the transferred distance and the implant distance). Note that, although the $|S_{21}|$ improvement of this work is 4.1 and 0.58 dB smaller than the improvement reported by Li et al. [16] and Shaw et al. [25], the implant distance of this work is almost seven and ten times deeper than it was in their study. Moreover, in [16], at an implant distance of only 3 mm, the application is severely limited, and the 430 MHz operating frequency makes it difficult to realize miniaturization in the design of implant devices.

TABLE VII
COMPARISONS OF THE PROPOSED WPT SYSTEM WITH PREVIOUS WORKS

Ref.	Operating Frequency	Tx Type	Rx Type	Transferred Distance [mm]	Implant Distance [mm]	$|S_{21}|$ Original System [dB]	$|S_{21}|$ Improvement [dB]	Experimental Environment
[24], 2014	2.45 GHz	Dipole	IFA	50	4	- 27.1	None	BTSL*
[16], 2018	430 MHz	Print coil	Print coil	63	3	- 45.9	15.7	BTSL
[21], 2018	2.45 GHz	Patch array	Folded diploe	20	10	- 40.05	5.17	Block of pork
[20], 2018	2.4 GHz	Monopole	Patch	130	130	- 88.31	None	Animal (pig)
[23], 2019	916.5 MHz	LPDA*	Planar IFA*	50	10	- 46.1	6.2	Minced pork
[26], 2019	2.45 GHz	Patch	Loop	53	5	- 18.98	5.94	BTSL
[22], 2020	915 MHz	Slot array	Print coil	50	≈ 50	- 32	4	Minced pork
[25], 2021	2.45 GHz	Patch	Slot	42	2	- 43.85	12.18	Minced pork
This work	**2.45 GHz**	**Dipole**	**Dipole**	**90**	**20**	**- 43.6**	**11.6**	**HBEL***

*BTSL—Body Tissue Simulating Liquids (self-made or commercial product). *LPDA—Logarithmic Periodic Dipole Antenna. *IFA—Inverted-F antenna.
*HBEL—BTSL of SPEAG, simulating muscle tissues.

Finally, it should be noted that the advantageous results obtained in this investigation were obtained by the use of a fundamental type of dipole antenna and not the well-designed antennas used in other works. The effectiveness of the proposed systematic method would not be affected by using different antenna types of Tx and Rx. It is likely that the WPT system can be further enhanced by switching the dipole antenna to another well-designed high-directivity antenna or using a more sophisticated array.

V. CONCLUSION

For the first time, a systematic method was successfully used to analyze the application of the WPT process to biomedical devices. In this investigation, we proposed and experimentally verified a systematic method for improving the efficiency of WPT technology applied to implantable biomedical devices. It was first revealed that the two causes of the high propagation loss in typical WPT scenarios were in-tissue attenuation and interface reflection. To counteract these issues, the use of a systematic method was presented as a means of comprehensively improving transmission efficiency. Two single methods, FZP and AL-AML, were proposed to reduce in-tissue attenuation and interface reflection, respectively, and were then combined to form the proposed systematic method. The performance of the proposed systematic method and its superiority over single methods was then carefully verified by simulation and experimental results.

Although this article has focused on the effectiveness validation of the systematic method, adopting different antennas such as Tx and Rx may have the potential to enhance the WPT efficiency. The study of design and optimization of specific Tx and Rx is beyond the scope of this article and is remaining as a future work.

The main results of this investigation are given as follows.

1) Experimentally, the proposed systematic method was shown to increase $|S_{21}|$ by a factor of 14.45 (11.6 dB) over that of the original system (which only contains an out-tissue Tx and an in-tissue Rx) and increase the relative maximum received power by 15.8 times (12 dB) that of the original system when the spacing distance is 90 mm and the implant depth is 20 mm.

2) Compared to the original system, the improvement of $|S_{21}|$ and τ was shown to be only 5.9 and 6 dB for the FZP, and 3.9 and 3.9 dB for the AL-AML. These results directly reveal the superiority of the proposed systematic methods over conventional single methods.

3) The proposed WPT system is shown to perform well when faced with the problem of misalignment of the implantable Rx in practical applications.

There is no doubt that the WPT efficiency of the proposed system could be further enhanced by improving the characteristic of the antenna and optimizing the performance of FZP and AL-AML. The systematic method proposed in this investigation represents a novel and effective guiding methodology in WPT research related to biological tissue and provides the basis for opening new avenues for further developments of an efficient WPT system for application to implantable devices.

REFERENCES

[1] R. Bashirullah, "Wireless implants," *IEEE Microw. Mag.*, vol. 11, no. 7, pp. S14–S23, Dec. 2010.

[2] T. Sun, X. Xie, and Z. Wang, "Design challenges of the wireless power transfer for medical microsystems," in *Proc. IEEE Int. Wireless Symp. (IWS)*, Apr. 2013, pp. 1–4.

[3] J. Lee and S. Nam, "Fundamental aspects of near-field coupling small antennas for wireless power transfer," *IEEE Trans. Antennas Propag.*, vol. 58, no. 11, pp. 3442–3449, Nov. 2010.

[4] R. Jegadeesan, K. Agarwal, Y.-X. Guo, S.-C. Yen, and N. V. Thakor, "Wireless power delivery to flexible subcutaneous implants using capacitive coupling," *IEEE Trans. Microw. Theory Techn.*, vol. 65, no. 1, pp. 280–292, Jan. 2017.

[5] R. Bosshard, J. Mühlethaler, J. W. Kolar, and I. Stevanović, "Optimized magnetic design for inductive power transfer coils," in *Proc. 28th Annu. IEEE Appl. Power Electron. Conf. Expo. (APEC)*, Mar. 2013, pp. 1812–1819.

[6] Y.-S. Seo, M. Quoc Nguyen, Z. Hughes, S. Rao, and J.-C. Chiao, "Wireless power transfer by inductive coupling for implantable batteryless stimulators," in *IEEE MTT-S Int. Microw. Symp. Dig.*, Jun. 2012, pp. 1–3.

[7] A. Kurs, A. Karalis, R. Moffatt, J. D. Joannopoulos, P. Fisher, and M. Soljačić, "Wireless power transfer via strongly coupled magnetic resonances," *Science*, vol. 317, no. 5834, pp. 83–86, 2007.

[8] J. Gozalvez, "WiTricity-the wireless power transfer [mobile radio]," *IEEE Veh. Technol. Mag.*, vol. 2, no. 2, pp. 38–44, Jun. 2007.

[9] Z. Wang, X. Wei, and H. Dai, "Principle elaboration and system structure validation of wireless power transfer via strongly coupled magnetic resonances," in *Proc. IEEE Vehicle Power Propuls. Conf. (VPPC)*, Oct. 2013, pp. 1–6.

[10] X. Zhang, S. L. Ho, and W. N. Fu, "Quantitative analysis of a wireless power transfer cell with planar spiral structures," *IEEE Trans. Magn.*, vol. 47, no. 10, pp. 3200–3203, Oct. 2011.

[11] M. R. Basar, M. Y. Ahmad, J. Cho, and F. Ibrahim, "An improved wearable resonant wireless power transfer system for biomedical capsule endoscope," *IEEE Trans. Ind. Electron.*, vol. 65, no. 10, pp. 7772–7781, Oct. 2018.

[12] R. Das and H. Yoo, "A multiband antenna associating wireless monitoring and nonleaky wireless power transfer system for biomedical implants," *IEEE Trans. Microw. Theory Techn.*, vol. 65, no. 7, pp. 2485–2495, Jul. 2017.

[13] C. Liu, C. Jiang, J. Song, and K. T. Chau, "An effective sandwiched wireless power transfer system for charging implantable cardiac pacemaker," *IEEE Trans. Ind. Electron.*, vol. 66, no. 5, pp. 4108–4117, May 2019.

[14] Y. Fan, L. Li, S. Yu, C. Zhu, and C.-H. Liang, "Experimental study of efficient wireless power transfer system integrating with highly sub-wavelength metamaterials," *Prog. Electromagn. Res.*, vol. 141, pp. 769–784, 2013.

[15] B. Wang, K. H. Teo, T. Nishino, W. Yerazunis, J. Barnwell, and J. Zhang, "Experiments on wireless power transfer with metamaterials," *Appl. Phys. Lett.*, vol. 98, no. 25, 2011, Art. no. 254101.

[16] L. Li, H. Liu, H. Zhang, and W. Xue, "Efficient wireless power transfer system integrating with metasurface for biological applications," *IEEE Trans. Ind. Electron.*, vol. 65, no. 4, pp. 3230–3239, Apr. 2018.

[17] A. S. Y. Poon, S. O'Driscoll, and T. H. Meng, "Optimal frequency for wireless power transmission into dispersive tissue," *IEEE Trans. Antennas Propag.*, vol. 58, no. 5, pp. 1739–1750, May 2010.

[18] S. A. A. Shah and H. Yoo, "Radiative near-field wireless power transfer to scalp-implantable biotelemetric device," *IEEE Trans. Microw. Theory Techn.*, vol. 68, no. 7, pp. 2944–2953, Jul. 2020.

[19] J. S. Ho, S. Kim, and A. S. Y. Poon, "Midfield wireless powering for implantable systems," *Proc. IEEE*, vol. 101, no. 6, pp. 1369–1378, Jun. 2013.

[20] P. Bose, A. Khaleghi, M. Albatat, J. Bergsland, and I. Balasingham, "RF channel modeling for implant-to-implant communication and implant to subcutaneous implant communication for future leadless cardiac pacemakers," *IEEE Trans. Biomed. Eng.*, vol. 65, no. 12, pp. 2798–2807, Dec. 2018.

[21] Z. Nie and Y. Yang, "A model independent scheme of adaptive focusing for wireless powering to in-body shifting medical device," *IEEE Trans. Antennas Propag.*, vol. 66, no. 3, pp. 1497–1506, Mar. 2018.

[22] K. Zhang et al., "Near-field wireless power transfer to deep-tissue implants for biomedical applications," *IEEE Trans. Antennas Propag.*, vol. 68, no. 2, pp. 1098–1106, Feb. 2020.

[23] S. Bakogianni and S. Koulouridis, "A dual-band implantable rectenna for wireless data and power support at sub-GHz region," *IEEE Trans. Antennas Propag.*, vol. 67, no. 11, pp. 6800–6810, Nov. 2019.

[24] C. Liu, Y.-X. Guo, H. Sun, and S. Xiao, "Design and safety considerations of an implantable rectenna for far-field wireless power transfer," *IEEE Trans. Antennas Propag.*, vol. 62, no. 11, pp. 5798–5806, Nov. 2014.

[25] T. Shaw, G. Samanta, and D. Mitra, "Efficient wireless power transfer system for implantable medical devices using circular polarized antennas," *IEEE Trans. Antennas Propag.*, vol. 69, no. 7, pp. 4109–4122, Jul. 2021.

[26] T. Shaw and D. Mitra, "Metasurface-based radiative near-field wireless power transfer system for implantable medical devices," *IET Microw., Antennas Propag.*, vol. 13, no. 12, pp. 1974–1982, Oct. 2019.

[27] Z. Zhang, H. Pang, A. Georgiadis, and C. Cecati, "Wireless power transfer—An overview," *IEEE Trans. Ind. Electron.*, vol. 66, no. 2, pp. 1044–1058, Feb. 2019.

[28] P. Nepa and A. Buffi, "Near-field-focused microwave antennas: Near-field shaping and implementation," *IEEE Antennas Propag. Mag.*, vol. 59, no. 3, pp. 42–53, Jun. 2017.

[29] S. Karimkashi and A. A. Kishk, "Focusing properties of Fresnel zone plate lens antennas in the near-field region," *IEEE Trans. Antennas Propag.*, vol. 59, no. 5, pp. 1481–1487, May 2011.

[30] F. Tofigh, J. Nourinia, M. Azarmanesh, and K. M. Khazaei, "Near-field focused array microstrip planar antenna for medical applications," *IEEE Antennas Wireless Propag. Lett.*, vol. 13, pp. 951–954, 2014.

[31] W. Wu, K.-D. Xu, Q. Chen, T. Tanaka, M. Kozai, and H. Minami, "A wideband reflectarray based on single-layer magneto-electric dipole elements with 1-bit switching mode," *IEEE Trans. Antennas Propag.*, vol. 70, no. 12, pp. 12346–12351, Dec. 2022.

[32] A. Basir and H. Yoo, "Efficient wireless power transfer system with a miniaturized quad-band implantable antenna for deep-body multitasking implants," *IEEE Trans. Microw. Theory Techn.*, vol. 68, no. 5, pp. 1943–1953, May 2020.

[33] F. Yang, J. Luo, S. Xu, and M. Li, "Design of artificial matching layers with arbitrary permittivity using a metasurface," *IEEE Antennas Wireless Propag. Lett.*, vol. 17, no. 8, pp. 1445–1448, Aug. 2018.

[34] T. Yilmaz, T. Karacolak, and E. Topsakal, "Characterization and testing of a skin mimicking material for implantable antennas operating at ISM band (2.4 GHz-2.48 GHz)," *IEEE Antennas Wireless Propag. Lett.*, vol. 7, pp. 418–420, 2008.

[35] *Basic Information of HBEL From SPEAG's Official Website*. Accessed: Feb. 1, 2023. [Online]. Available: https://speag.swiss/components/materials-liquids/msl/

[36] D. N. Black and J. C. Wiltse, "Millimeter-wave characteristics of phase-correcting Fresnel zone plates," *IEEE Trans. Microw. Theory Techn.*, vol. MTT-35, no. 12, pp. 1122–1129, Dec. 1987.

[37] F. A. Jenkins and H. E. White, *Fundamentals of Optics*. New York, NY, USA: McGraw-Hill, 1957, pp. 385–386.

[38] J. D. Kraus and D. A. Fleisch, *Electromagnetics*. New York, NY, USA: McGraw-Hill, 1999, pp. 509–511.

[39] Q. Yuan and S. Suzuki, "Exact matching approach with circuit element ohmic loss," in *Proc. Int. Symp. Antennas Propag. (ISAP)*, 2016, pp. 342–343.

[40] S. Suzuki, Q. Yuan, and Q. Chen, "Impedance matching approach of L-section circuit with ohmic loss in reactive components," *Wireless Power Transf.*, vol. 5, no. 1, pp. 64–74, Mar. 2018.

[41] Q. Chen, K. Ozawa, Q. Yuan, and K. Sawaya, "Antenna characterization for wireless power-transmission system using near-field coupling," *IEEE Antennas Propag. Mag.*, vol. 54, no. 4, pp. 108–116, Aug. 2012.

[42] Y. Li, H. Sato, and Q. Chen, "Capsule antenna design based on transmission factor through the human body," *IEICE Trans. Commun.*, vol. 101, no. 2, pp. 357–363, 2018.

[43] C. Chou, *IEEE Standard for Safety Levels With Respect to Human Exposure to Radio Frequency Electromagnetic Fields, 3 kHz to 300 GHz*, IEEE Standard c95.1-2005, The Institute of Electrical and Electronics Engineers, New York, NY, USA, 2006.

[44] R. Meys and F. Janssens, "Measuring the impedance of balanced antennas by an S-parameter method," *IEEE Antennas Propag. Mag.*, vol. 40, no. 6, pp. 62–65, Dec. 1998.

[45] T. Fukasawa, T. Yanagi, H. Miyashita, and K. Konishi, "Extended S-parameter method including radiation pattern measurements of an antenna," *IEEE Trans. Antenna Propag.*, vol. 60, no. 12, pp. 5645–5653, Dec. 2012.

[46] K. Fukunaga, S. Watanabe, and Y. Yamanaka, "Dielectric properties of tissue-equivalent liquids and their effects on specific absorption rate," *IEEE Trans. Electromagn. Compat.*, vol. 46, no. 1, pp. 126–129, Feb. 2004.

Xianbo Cao (Graduate Student Member, IEEE) was born in Xi'an, Shaanxi, China, in 1995. He received the B.S. and M.S. degrees in electromagnetic field and microwave technology from Xidian University, Xi'an, China, in 2016 and 2019, respectively. He is currently pursuing the Ph.D. degree with the Department of Communications Engineering, Tohoku University, Sendai, Japan.

His current research interests include wireless power transfer (WPT), metasurfaces, time-modulated arrays, reflectarray antennas, and reconfigurable intelligent surfaces (RISs).

Mr. Cao was a recipient of the Best Student Award at the 2018 Asian Wireless Power Transfer Workshop (AWPT 2018) in 2018.

Hiroyasu Sato (Member, IEEE) received the B.E. and M.E. degrees from Chuo University, Tokyo, Japan, in 1993 and 1995, respectively, and the D.E. degree from Tohoku University, Sendai, Japan, in 1998.

He is currently an Assistant Professor with the Department of Communications Engineering, Tohoku University. His current research interests include the experimental study of electromagnetic waves, computational electromagnetics, antennas in plasma, antennas for plasma production, broadband antennas, wireless power transfer, and active/passive millimeter-wave imaging.

Dr. Sato is a member of the Institute of Electronics, Information and Communication Engineers (IEICE). He received the First Place of the Best Paper Award from the International Symposium on Antennas and Propagation (ISAP) in 2017.
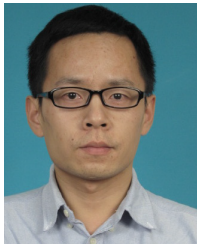
Kai-Da Xu (Senior Member, IEEE) received the B.E. and Ph.D. degrees in electromagnetic field and microwave technology from the University of Electronic Science and Technology of China (UESTC), Chengdu, China, in 2009 and 2015, respectively.

From 2012 to 2014, he was a Visiting Researcher with the Department of Electrical and Computer Engineering, Duke University, Durham, NC, USA, under financial support from the China Scholarship Council. In 2015, he joined the Department of Electronic Science, Xiamen University, Xiamen, China, as an Assistant Professor. From 2016 to 2017, he was a Post-Doctoral Fellow with the State Key Laboratory of Millimeter Waves, City University of Hong Kong, Hong Kong. From 2018 to 2019, he was an Honorary Fellow with the Department of Electrical and Computer Engineering, University of Wisconsin–Madison, Madison, WI, USA. He was successfully selected into the Youth Talent Support Program of Xi'an Jiaotong University (XJTU) in 2019, and joined the School of Information and Communications Engineering at XJTU in 2020. Also, he was awarded a fellowship from the Japan Society for the Promotion of Science (JSPS) and was a JSPS Fellow with the Department of Communications Engineering, Tohoku University, Sendai, Japan, from November 2019 to May 2021. He has authored or coauthored over 160 papers in peer-reviewed journals and over 50 papers in conference proceedings. His current research interests include RF/microwave, mm-wave/THz devices, and antenna arrays.

Wen Jiang (Member, IEEE) was born in Shandong, China, in 1985. He received the B.S. and Ph.D. degrees from Xidian University, Xi'an, China, in 2008 and 2012, respectively.

He is currently the Vice-Director of the National Key Laboratory of Science and Technology on Antennas and Microwaves, Xidian University, where he is also a Full Professor. His current research interests include electromagnetic scattering theory and technology, antenna theory and engineering, and electromagnetic measurement theory technology.

Shuxi Gong (Member, IEEE) was born in Hebei, China, in March 1957. He received the B.S. and M.S. degrees from Xidian University, Xi'an, China, in 1982 and 1984, respectively, and the Ph.D. degree from Xi'an Jiaotong University, Xi'an, in 1988.

He was the Director of the National Key Laboratory of Science and Technology on Antennas and Microwaves, Xidian University, where he is currently a Full Professor. He has authored or coauthored over 200 refereed journal articles. His current research interests include antenna theory and technology, and electromagnetic scattering theory and technology.

Qiang Chen (Senior Member, IEEE) received the B.E. degree from Xidian University, Xi'an, China, in 1986, and the M.E. and D.E. degrees from Tohoku University, Sendai, Japan, in 1991 and 1994, respectively.

He is currently a Chair Professor with the Electromagnetic Engineering Laboratory, Department of Communications Engineering, Faculty of Engineering, Tohoku University. His primary research interests include antennas, microwaves and millimeter waves, electromagnetic measurement, and computational electromagnetics.

Dr. Chen is a fellow of the Institute of Electronics, Information and Communication Engineers (IEICE). He received the Best Paper Award and the Zen-ichi Kiyasu Award from IEICE. He has served as the Chair of the IEICE Technical Committee on Photonics-Applied Electromagnetic Measurement from 2012 to 2014, the IEICE Technical Committee on Wireless Power Transfer from 2016 to 2018, the IEEE Antennas and Propagation Society Tokyo Chapter from 2017 to 2018, and the IEICE Technical Committee on Antennas and Propagation from 2019 to 2021.